Laboratory Experiments for Tsunamis Generated by Underwater Landslides: Comparison with Numerical Modeling

François Enet [1], Stéphan T. Grilli [1] and Philip Watts [2]
1. Department of Ocean Engineering, University of Rhode Island, Narragansett, RI, USA
2. Applied Fluids Engineering, Inc., Long Beach, CA, USA

ABSTRACT

Three-dimensional experiments and fully nonlinear computations are performed at the University of Rhode Island, to investigate tsunami generation by underwater landslides. Each experiment consists of a solid landslide of idealized smooth shape sliding over a plane slope. Surface elevations are measured using very accurate gages placed at strategic locations. Gage calibration is performed using a newly developed automated system. Landslide acceleration is measured with a micro-accelerometer. The repeatability of experiments is first investigated, and then by varying the initial depth of the landslide, different conditions of wave non-linearity and dispersion are generated and compared. The principle of numerical modeling, using an earlier developed model, is briefly explained. One application is presented and results compared to experiments. The agreement of computations with the latter is quite good. In the model, horizontal velocities are found quite non-uniform over depth above the moving landslide. This would preclude using a long wave model for such landslide tsunami wave generation.

KEY WORDS: Tsunamis; landslides; experiments; numerical wave tank; Boundary Element Method.

INTRODUCTION

For many coastal areas, underwater landslides represent one of the most dangerous mechanisms for tsunami generation. Whereas tsunamis directly generated by coseismic displacement are generally of small amplitude, and correlate well with moment magnitude, tsunamis generated by submarine landslides are only limited by the vertical extent of landslide motion (Murty, 1979; Watts 1997, 1998). Moreover, underwater landslides can be triggered by moderate earthquakes (Tappin et al, 1999; Tappin et al, 2001) and often occur on the continental slope. Hence, such landslide tsunamis offer little time for warning a local populations. Thus the so-called 1946 Unimak tsunami (Fryer et al., 2001) was generated by a giant underwater landslide (200 km^3), triggered by a Ms $\approx$ 7.1 earthquake. The landslide moved down a 4 degree slope from an initial headwall depth of 150 m to the 6000 m depth of the Aleutian terrace. The coastal runup was estimated at 35 m above sea level, at a small distance just onshore of the landslide generation area. The large coastal hazard posed by landslide tsunamis justifies the need for identifying sensitive sites and accurately predicting possible landslide tsunami scenarii and amplitudes.

The methods used for predicting landslide tsunami amplitudes are of three types: (i) laboratory experiments; (ii) analytical descriptions; and (iii) numerical simulations. Work based on laboratory experiments and analytical descriptions has been documented, e.g., by Wiegel (1955), Iwasaki (1982), Heinrich (1992), and Watts (1997, 1998, 2000). Two-dimensional numerical simulations, based on linear wave theory, have been proposed by Iwasaki (1987, 1997) and Harbitz (1992). Heinrich (1992) and Assier-Rzadkiewicz et al. (1997) used a volume of fluid (VOF) solution of Navier Stokes equations in their two-dimensional (2D) simulations, and Verriere and Lenoir (1992) used linearized potential flow equations. Nonlinear shallow water wave equations (NSW) were used by Jiang and Leblond (1992, 1993, 1994), Imamura and Gica (1996) and Fine et al. (1998). The wavemaker formalism developed by Watts (1998) was applied to a 2D fully nonlinear potential flow (FNPF) model by Grilli and Watts (1999) and validated with experimental results, e.g., in Watts, et al. (2000). The same formalism was implemented in a 3D FNPF model by Grilli, et al. (2002). This three-dimensional (3D) Numerical Wave Tank (NWT) has been validated both numerically and experimentally by Grilli et al. (2000, 2001), for solitary wave shoaling and breaking over slopes.

Here, we describe new 3D laboratory experiments of underwater landslide tsunami generation. These experiments are carried out both to gain physical insight into and further validate the 3D-FNPF NWT used for landslide tsunami generation by Grilli et al. (2002). We present preliminary results for these experiments and briefly detail the numerical model. One application of the numerical model to an experimental configuration is finally presented and results are compared with experiments.

EXPERIMENTAL SET UP

General model set up

Experiments are set-up in the 3.7 m wide, 1.8 m deep and 30 m long wave tank of the Ocean Engineering Department at the University of Rhode Island. The set up includes a plane aluminum incline, placed in the tank at a 15 degree angle (Figs. 1-3). A solid landslide model translates down the slope under the action of gravity, while being guided by a small rail. The displacement of the landslide parallel to the slope is measured by a micro-accelerometer embedded at the landslide's center of mass. Generated surface waves are measured using capacitance wave gages.

Tank incline

The tank was already equipped with an adjustable beach, but the beach geometry did not meet our needs Hence, we built a new incline over the existing beach, 15 m long by 3.7 m wide, made of riveted aluminum plates supported by a series of I-beams (Fig. 1). This assembly provided us with a very rigid platform on which to operate our landslide model. The accuracy of the specified slope angle was a critical parameter for the quality of the measured results and we gave it special attention. In order to adjust the incline, we first positioned the beam supporting the structure, across the tank, to its position. We then corrected the slight sagging of the structure under its weight with a jack located in the center of the submerged part of the slope, and two adjustable threaded rods on each side of the tank. To measure the slope angle, we used a transit and metallic squares as references. The angle of the slope obtained was found to be 15 º (± 3 ').

Landslide model

The landslide model was built out of aluminum sheets, bolted and glued together (Figs. 1 and 2). The landslide model geometry was defined using truncated hyperbolic secant functions of x and y as (Fig. 4),

$$z(x,y) = \frac{T}{r}\left[\operatorname{sech}(K_w x)\operatorname{sech}(K_b y) - (1-r)\right] \quad ; \text{for } z \geq 0 \quad (1a)$$

with,

$$K_w = \frac{2}{w}\operatorname{asech}\left(\frac{1-r}{r}\right) \quad \text{and} \quad K_b = \frac{2}{b}\operatorname{asech}\left(\frac{1-r}{r}\right) \quad (1b)$$

with the ratio of truncation $r = 0.6$, the landslide maximum thickness $T = 80$ mm, the landslide length $b = 400$ mm, and width $w = 700$ mm. Using Eq. (1), we find the landslide model theoretical volume $V_b = 5.505 \ 10^{-3} \ m^3$ and, weighing the model, the model bulk density $\rho_b = 2,700$ kg/m^3. The landslide was built to slide on a guiding rail (Fig. 2) and a fishing reel was used to move the landslide up and down the slope in between experiments (Fig. 1). To initiate an experiment, the quick release mechanism of the fishing reel was used to let go of the landslide. In order to avoid disturbances on the free surface, the metallic cable connecting the landslide to the fishing reel was run through a piece of tubing bolted to the rail and piercing the free surface.

A cavity was built within the landslide to accommodate a carriage and the accelerometer. The carriage both supported the landslide on the rail using bearings and provided lateral guidance to the body, to avoid any lateral motion.
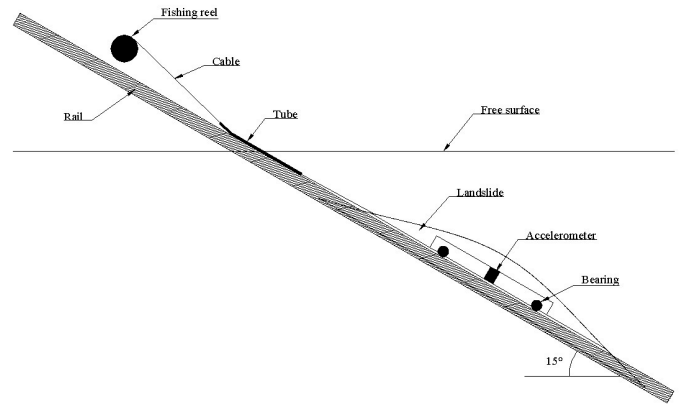

Fig. 1: Cross-section in landslide model and incline (heights are exaggerated).

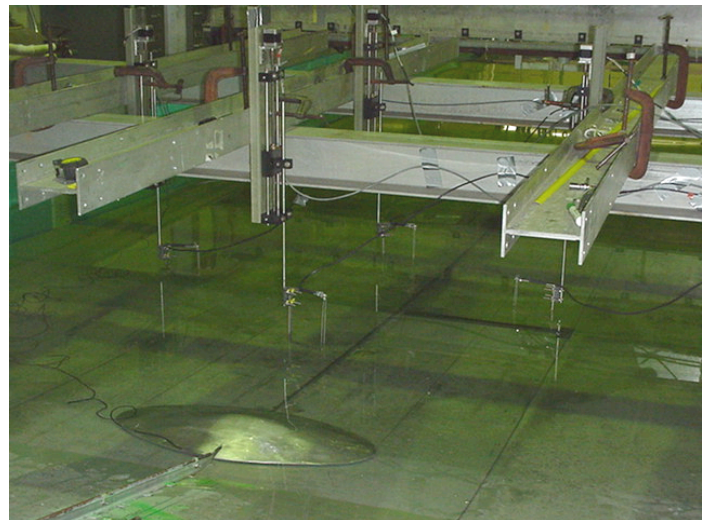Fig. 2: Landslide resting on top of the guiding rail

Fig. 3: General view of experimental set up, incline, landslide model, wave gages and supporting I-beams.

To prevent the body from tilting, small curve shape springs were fixed on both sides and in front of the landslide bottom. The landslide motion was stopped at the bottom of the slope by a foam cushion.

Instrumentation

During experiments we continuously measured the landslide acceleration and free surface elevation at gages. The acceleration was measured with a micro-accelerometer Kystler 8305A2M2. The accelerometer was placed at the location of the landslide center of mass (Fig. 1). The wire, connecting the accelerometer to the data acquisition system exited the landslide from the rear (Fig. 3).

Surface elevations were measured using a set of four capacitance gages WG-50 built by Brancker Research Ltd. The absolute accuracy of these gage measurements was 0.4 mm. Both accelerometer and gage signals were collected, through an acquisition card, usually at a 100 Hz frequency, and stored in a computer.

The gage calibration required special attention because environmental conditions could vary during experiments (e.g., ambient temperature). Hence, gages had to be frequently calibrated. To do so, we built four computer operated step motor systems to remotely perform in situ gage calibration by moving gages up or down with great vertical accuracy and recording the voltage variation. Each gage is bolted at the end of a motor shaft and the whole system is clamped on supporting I-beams (Fig. 3). The displacement obtained with the step motor system has an absolute accuracy of 0.1 mm. To reduce the meniscus effect on the gage records, silicon was sprayed on the gage wires. During the experiments, the quality of the water also appeared to be of real importance. We found that increased viscosity due to micro-organisms (phytoplankton) residing in the upper layer of the tank could corrupt the data. This problem was mitigated by constantly filtering the wave tank water and periodically adding chlorine to it.
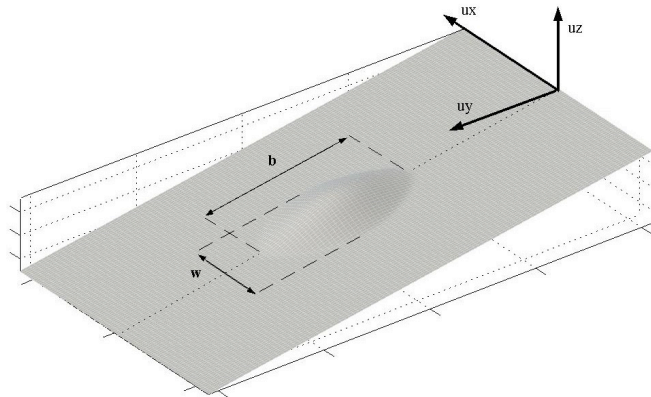

Fig. 4: Coordinate system for the experimental set-up

The horizontal positioning of gages is an important parameter for the comparison of measurements with numerical results. The I-beams supporting the apparatus were used as a rigid frame for the positioning of gages. Measuring tape was affixed to the beams, and a string running between the beams at the desired location and a plumb line were used to position the gages. We obtained an accuracy of less than 1 mm in horizontal gage positioning. The reference frame used for the experiments is described in Fig. 4. In the same manner, the water depth in the tank was measured on a daily basis with the plumb line and kept as close as possible to 1.5 m. Before performing an experiment, the initial position and depth of the landslide were first determined using

the plumb line. Then, to reposition the landslide during one set of experiments without disturbing the free surface, a metallic rod was placed on the slope, one end touching the landslide, the other end used as reading mark on a measuring tape fixed on the dry part of the beach. The water depth h_o and the landslide initial depth were measured within 1 mm.

So far, the landslide has been positioned only at three different initial depths, $d = 70$, 150 and 220 mm, in order to investigate the repeatability of the landslide motion and symmetry with respect to y of the generated waves. Comparisons with numerical results are presented in the following for $d = 70$ mm.

EXPERIMENTAL RESULTS

Our main concern was to verify the repeatability of experiments. To do so, we compared the motion of the landslide for different runs and the generated free surface waves.

Landslide law of motion

To analyze data from the micro-accelerometer, we follow Watts and Grilli (2003) and assume that bottom friction under the landslide is negligible as compared to hydrodynamic drag on the moving landslide. This yields the following law of motion for a semi-ellipsoidal landslide center of mass motion, s, parallel to the slope,

$$\left(\rho_b + C_m \rho_w\right) V_b \frac{d^2 s}{dt^2} \approx \left(\rho_b - \rho_w\right) V_b \, g\sin\theta - \frac{1}{2} C_d \, \rho_w \, A \left(\frac{ds}{dt}\right)^2 \quad (2)$$

where ρ_w is the water density, C_m is an added mass coefficient, C_d is a drag coefficient, A is the landslide main cross-sectional area, and θ is the slope angle. Assuming $s = 0$, $ds/dt = 0$, and $d^2s/dt^2 = a_0$, at time $t = 0$, as well as $ds/dt \approx u_t$ and acceleration $d^2s/dt^2 \approx 0$ for large times, Eq. (2) leads to non-dimensional initial acceleration and terminal velocity,

$$\frac{a_o}{g} = \frac{\gamma - 1}{\gamma + C_m} \, \sin\theta \quad (3)$$

$$\frac{u_t}{\sqrt{gb}} = \sqrt{\frac{4(\gamma - 1)}{3C_d} \, \sin\theta} \quad (4)$$

respectively, where $\gamma = \rho_b / \rho_w$ is the landslide specific density. Using Eqs. (3) and (4), the exact solution of Eq. (2) can be expressed as,

$$s = s_0 \, \ln\left[\cosh\left(\frac{t}{t_0}\right)\right] \quad (5)$$

Based on this, the speed and acceleration of the landslide center of mass are:

$$\dot{s} = u_t \, \tanh\left(\frac{t}{t_0}\right) \quad (6)$$

$$\ddot{s} = a_0 \, \cosh\left(\frac{t}{t_0}\right)^{-2} \quad (7)$$

With:

$$s_0 = \frac{u_t^2}{a_0} \quad (8)$$

and

$$t_0 = \frac{u_t}{a_0} \qquad (9)$$

a characteristic distance of landslide motion and a characteristic duration of landslide motion, respectively.

Free surface elevation

An example of measured free surface elevation is shown in Fig. 5. The picture clearly shows a succession of cylindrical waves propagating away from the landslide, in the direction of its motion. At the stage of Fig. 5, a main crest can be seen, leading a train of smaller waves. There is less wave propagation towards the sides of this main crest, but the train of smaller waves following it is more cylindrical. Pictures taken at earlier times would show that a large depression wave first forms above the initial location of the landslide, and then "rebounds" to form a main wave of elevation (i.e., the main crest). The depression wave rebound also propagates shoreward and reflects on the slope, causing some of the smaller waves seen to the left of the figure.
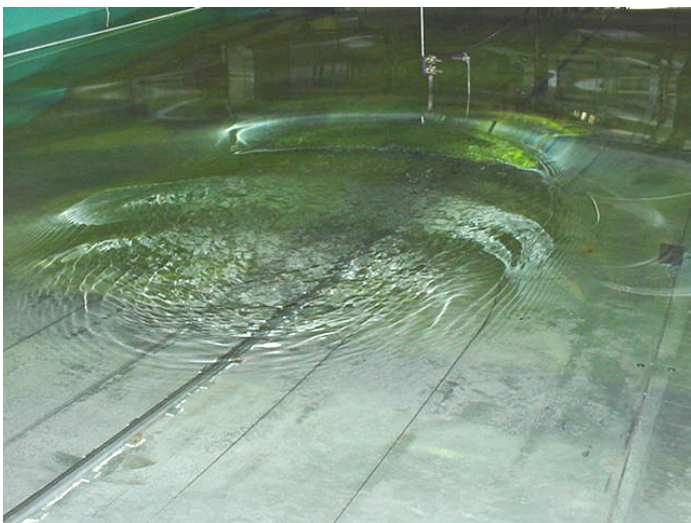

Fig. 5: Surface waves generated by the underwater landslide model in experiments run for $d = 0.07$ m.

Landslide kinematics

For each experiment, the micro-accelerometer records data for the landslide center of mass acceleration parallel to the slope, as a function of time. Acceleration is time integrated to provide velocity and twice time integrated to provide center of mass motion. From these, both a_0 and u_t are calculated. More specifically, selecting a small arbitrary time step to integrate the measured acceleration data, and using Eq. (5), we perform a curve fitting of the landslide motion s as a function of time, based on the least square method. This provides t_0 and s_0, from which a_0 and u_t are found using Eqs. (8) and (9). The time interval for the integration is then readjusted using the calculated parameter t_0, and, if needed, the curve fitting computations are repeated. An example of curve fitting is given in Fig. 6, for $d = 0.07$ m. We find, for $\rho_w = 1,000$ kg/m³, $\gamma = 2.7$, and $\theta = 15$ deg.: $t_0 = 1.92$ s, $s_0 = 3.558$ m, $a_0 = 0.961$ m/s² and $u_t = 1.849$ m/s. With these values, the theoretical law described by Eq. (5) fits the experimental data quite well. Using Eqs. (3) and (4), we finally find $C_m = 1.79$ and $C_d = 0.70$, which both are realistic values for a streamlined body.
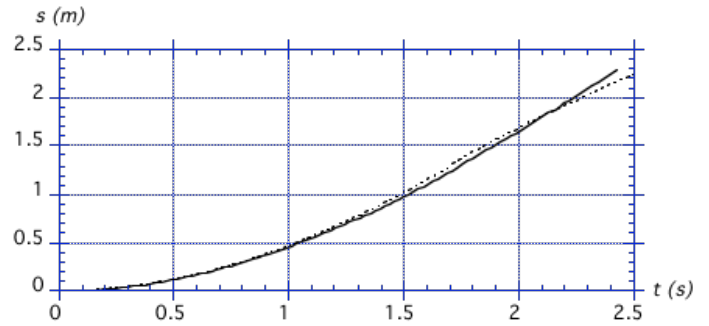

Fig. 6: Curve fitting with Eq. (5) (———) of experimental displacement (- - - -) (obtained by double integration of the average acceleration of runs 2-5 in Table 1), with $a_o = 0.961$ m/s², $u_t = 1.849$ m/s, $R^2 = 0.99$, for $\theta = 15$ deg., $d = 0.07$ m.
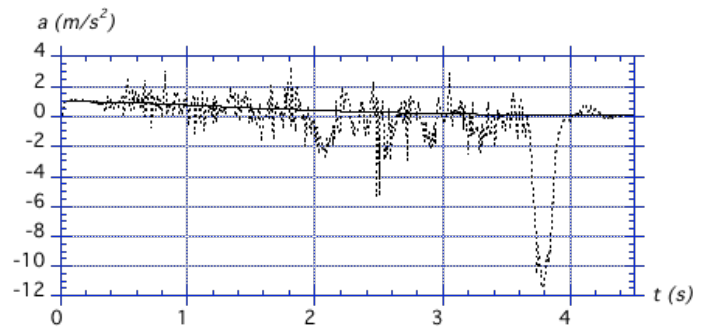

Fig. 7: Same case as Fig. 6. Comparison of the measured acceleration data (- - - -) (average of runs 2-5 in Table 1) and the theory (———) (Eq. 7).

Table 1: Values of a_0 and u_t for six different runs, with $d = 0.07$ m (standard deviation for $a_0 = 0.05$ m/s², standard deviation for $u_t = 0.26$ m/s).

Run #	1	2	3	4	5	6
a_0	0.8872	1.0415	0.9735	0.9883	0.9322	0.9745
u_t	1.772	1.7562	1.958	2.4565	1.8984	2.0521

Knowing a_0 and u_t, the theoretical velocity and acceleration over time can also be obtained from Eqs. (6) and (7). A comparison between an (unfiltered) experimental acceleration signal and its theoretical equivalent is shown in Fig. 7. Although, the experimental signal is very noisy, due to many small shocks happening during landslide motion on the slope, the theoretical acceleration follows its general trend quite well. The last (large negative) peak in the signal around 3.7 sec corresponds to the abrupt stop of the landslide in the foam cushion at the bottom of the slope.

Repeatability of experiments

The repeatability of experiments is first investigated through the comparison of measured landslide center of mass motion, i.e., the twice integrated landslide acceleration. Through the curve fitting procedure explained above, we compute initial acceleration a_0 and terminal velocity u_t for six runs with $d = 0.07$ m (Table 1), and find averages values of 0.966 m/s² and 1.982 m/s for each parameter, respectively, with standard coefficients of variation of 5% and 13%, respectively.

Clearly, the initial acceleration is more repeatable than the terminal velocity. This can be explained by the fact that the latter is affected by random shocks occurring during landslide motion (e.g., Fig. 7), whereas the former only depends on the repeatability of the landslide initial position and release mechanism (fishing reel). The average characteristic time is $t_o = 2.05$ s in this case. Since most of the tsunamigenic potential of the landslide occurs at early times, for $t < t_o$ (Watts, 1997,1998), the larger experimental variation on the terminal velocity should not affect wave generation in laboratory experiments too much.
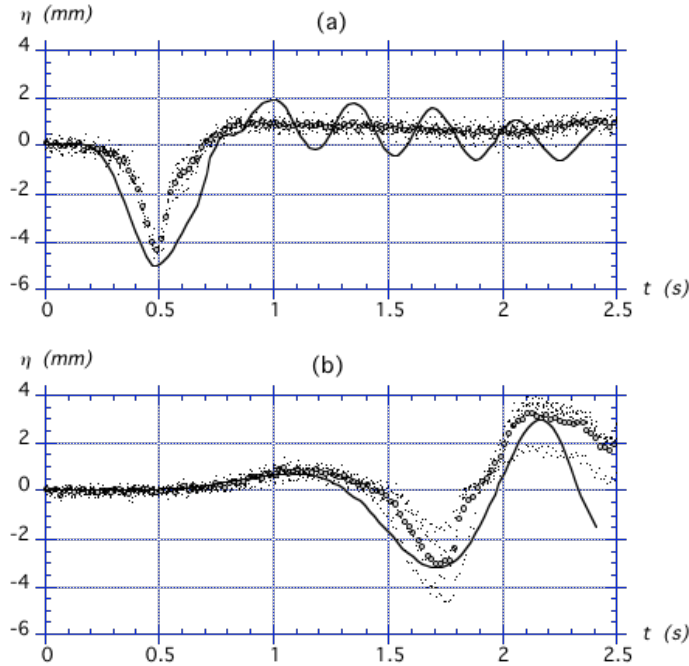

Fig. 8: Surface elevations measured for $d = 0.070$ m : (.) runs 2-5 in Table 1; and (o) average of those, at gages located at : (a) ux = 0, uy = 0.570 m; (b) ux = -0.682 m, uy = 1.498 m. Numerical simulations based on average landslide model motion (——) (Figs. 6 and 7).

We now compare free surface measurements at wave gages for replicates of model runs (2-5 in Table 1), with identical parameters, i.e., same initial depth of submergence $d = 0.07$ m. Before comparing wave gage records we first synchronized them in time by determining the initial instant of landslide motion ($t = 0$) from the acceleration record. Fig. 8a shows surface amplitudes measured at a wave gage located on the landslide axis, at the initial position of the landslide point of maximum thickness, at $y = 0.576$ m. Wave elevations are repeatable within 0.6-1.3 mm. Fig. 8b shows results for a gage located at x = -0.682 m and $y = 1.498$ m, i.e., away from the landslide axis. Here, we see larger differences between measurements made for different runs, of up to 3mm. Uncertainties on gage position and timing for wave arrival, however, are also larger.

In conclusion, considering the differences in landslide motion (Table 1), measured surface elevations for run replicates seem repeatable enough for their average to provide us with a good source of data for comparing with and validating our numerical model.

Symmetry of measured waves

For future experiments, it is desirable to know whether the generated wave field is truly symmetric with respect to the landslide axis. This will allow us to only use wave gages on one side of the axis of symmetry, thus increasing the amount of simultaneously recorded independent data. To assess wave field symmetry, we compare records for symmetrically located wave gages taken during the same run (Fig. 9). Although there are some discrepancies for the smaller waves (< 1 mm), likely due to measuring accuracy, t he wave is symmetric enough for its main features to allow us to place all the wave gages both on the axis of symmetry and on one side of this axis. As a consequence, we will be able to collect data at a greater number of locations, providing more points of comparison with the numerical model. In any case, for future experiments, the numerical model should also be used to determine strategic locations for wave gages, in order to obtain the most meaningful and significant data.
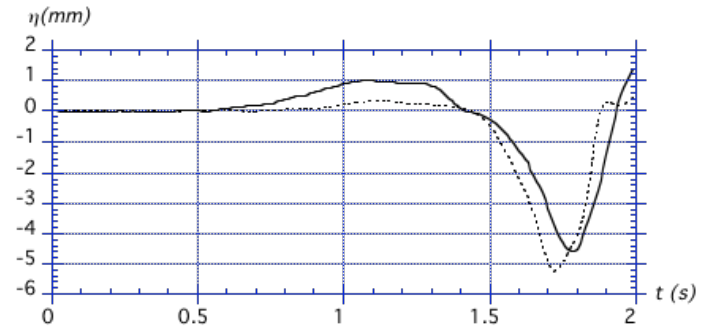

Fig. 9: Comparison for $d = 0.070$ m, of measurements at gages located at $y = 1.498$ m, and at the same distance from the axis of symmetry : (——) x = -0.682 m; (- - - -) $x = 0.682$m.

NUMERICAL MODELING

The numerical model used to simulate landslide tsunamis in a set-up similar to laboratory experiments is a three-dimensional (3D) Numerical Wave Tank (NWT) solving Fully Nonlinear Potential Flow (FNPF) theory, using a higher-order Boundary Element Method (BEM). Details of the model and its application to landslide tsunami simulations can be found in Grilli and Watts (1999), Grilli et al. (2001) and Grilli et al. (2002). Below is a brief summary of model equations and numerical implementation.

Governing Equations

The velocity potential, $\phi(\mathbf{x},t)$, describes the inviscid irrotationnal 3D flows in Cartesian coordinates $\mathbf{x} = (x,y,z)$, with z the upward vertical direction. The velocity is defined as $\mathbf{u} = \boldsymbol{\nabla}\phi = (u,v,w)$. Continuity equation for the fluid domain $\Omega(t)$, with boundary $\Gamma(t)$ is Laplace's equation for the potential,

$$\nabla^2 \phi = 0 \qquad \text{in} \quad \Omega(t) \tag{10}$$

Green's second identity transforms Eq. (10) into the boundary integral equation,

$$\alpha_l \phi_l = \int_\Gamma \left(\frac{\partial \phi}{\partial n}(\mathbf{x}) G(\mathbf{x},\mathbf{x}_l) - \phi(\mathbf{x}) \frac{\partial G}{\partial n}(\mathbf{x},\mathbf{x}_l) \right) d\Gamma \tag{11}$$

in which, $\alpha_l = \alpha(\mathbf{x}_l) = \dfrac{\theta_l}{4\pi}$, with θ_l the exterior solid angle of the boundary at point $\mathbf{x}_l$, and the 3D free space Green's functions defined as,

$$G = \frac{1}{4\pi r} \quad \text{with} \quad \frac{\partial G}{\partial n} = -\frac{1}{4\pi} \frac{\mathbf{r.n}}{r^3} \qquad (12)$$

where $\mathbf{r} = \mathbf{x} - \mathbf{x}_l$, $r = |\mathbf{r}|$, $\mathbf{x}$ and $\mathbf{x}_l = (x_l, y_l, z_l)$ are points on boundary Γ, and $\mathbf{n}$ is the outward unit vector normal to the boundary at point $\mathbf{x}$.

The computational domain boundary is divided into a number of sections, over which different boundary conditions are specified. On the free surface, the potential ϕ satisfies the non linear kinematic and dynamic free surface conditions,

$$\frac{D\mathbf{R}}{Dt} = \mathbf{u} = \nabla\phi \qquad \text{on the free surface} \qquad (13)$$

$$\frac{D\phi}{Dt} = -gz + \frac{1}{2}\nabla\phi.\nabla\phi - \frac{p_a}{\rho_w} \qquad \text{on the free surface} \qquad (14)$$

where $\mathbf{R}$ is the position vector of the free surface water particles, g the acceleration due to gravity, ρ_w the water density, and D/Dt the material derivative operator. No-flow boundary conditions are specified over the stationary parts of the boundary, especially on the lateral sides of the NWT:

$$\overline{\frac{\partial\phi}{\partial n}} = 0 \qquad (15)$$

Active absorbing boundary conditions are specified on the other extremities of the NWT, over which most of the generated tsunami wave energy impinges. These boundary conditions are modeled as vertical pressure sensitive 'snake' piston wave absorbers. The velocity on the piston boundary is defined as:

$$\overline{\frac{\partial\phi}{\partial n}} = u_{ap} \qquad (16)$$

with,

$$u_{ap}(\sigma,t) = \frac{1}{\rho_w h_o \sqrt{gh_o}} \int_{-h_o}^{\eta_{ap}(\sigma,t)} p_D(\sigma,z,t) \, dz \qquad (17)$$

the piston velocity calculated at the curvilinear abscissa σ, horizontally measured along the piston boundary, η_{ap} being the surface elevation at the piston and p_D the dynamic pressure (Grilli, et al., 2002).

The bottom boundary condition, for a specified underwater landslide geometry $\mathbf{x}_l$ and motion, is defined by the landslide center of mass motion (Eqs. (5) to (9)),

$$\overline{\mathbf{x}} = \mathbf{x}_l, \quad \overline{\frac{\partial\phi}{\partial n}} = \mathbf{u}_l \cdot \mathbf{n} = \frac{d\mathbf{x}_l}{dt} \cdot \mathbf{n} \qquad (18)$$

Free surface boundary conditions (13) and (14) are integrated at time t to establish both the new position and the boundary conditions on the free surface at time $t+\Delta t$. For further details, the interested reader is referred to Grilli *et al.* (2001, 2002).

Landslide geometry and motion

To compare numerical simulations with experiments, the NWT is set-up with landslide geometry and motion identical to those in experiments. Thus, the initial landslide geometry is defined by Eq. (1), expressed in the numerical model reference frame. The landslide geometry at time t in the NWT, to be used in Eq. (18), is then found as:

$$\mathbf{x}_l(t) = \mathbf{x}_l(0) - s(t) \, (\mathbf{i}\cos(\theta) + \mathbf{k}\sin(\theta)) \qquad (19)$$

where Eq. (5) is used to compute $s(t)$, the landslide law of motion. The center of mass velocity and acceleration follow from Eqs. (6) and (7).

In computations, parameters a_0 and u_t in Eqs. (8) and (9) are obtained from experimental model displacement curve fits, averaged over different runs with identical initial conditions (e.g., Fig. 6), and used in the law of motion. To describe the initial observed motion of the landslide, a ramp-up of the acceleration to a_0 has been implemented in the model, in the form of a tanh function varying over a small interval (order $t_o/20$). Also, because of the finite length of the slope, the landslide is decelerated at some point, to smoothly reach the bottom of the slope (see Grilli et al., 2002 for details).
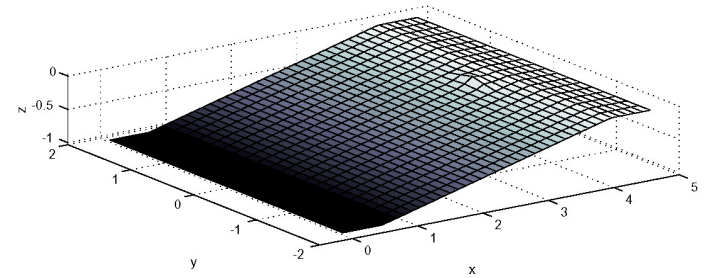

Fig. 10: NWT wave tank bottom discretization for tsunami landslide simulation of laboratory experiments, with $d = 0.07$ m. Note, the actual geometric interpolation in the NWT is bi-cubic

Application

To perform the experimental/numerical comparison we represent the experimental geometry in the model. Fig. 10 shows the bottom discretization in the NWT. Note that x and y axes are oriented differently than in Fig. 4. To limit the extent of the computational domain, we truncate the slope to a 1 m depth. As required in the model (see Grilli et al., 2002), we place two small shelves, 0.6 m long, both at the toe and at the top of the slope. The latter has a depth 0.06 m and represents a deviation from the experimental geometry, which may slightly influence results. Two vertical absorbing boundaries are located at each extremity in the x direction, on which we specify boundary conditions (16) and (17). Vertical boundaries in the y direction are impermeable, and we specify boundary condition (15). The landslide is initially located with its maximum thickness in depth $d = 0.07$ m, at $x = 3.754$ m and $y = 0$. The landslide dimensions and volume correspond to the experimental model. We use $a_0 = 0.961$ m/s^2 and $u_t = 1.849$ m/s, i.e., the average experimental values, in the law of motion to specify boundary condition (18) in the NWT (Fig. 6). Due to the shallower depth in the NWT, however, landslide deceleration is started at $t = 2.8$ s, whereas it starts at 3.7 s in experiments (Fig. 7). The bottom and free surface are discretized with 41 by 21 nodes leading to an initial grid size, $\Delta x = 0.118$ m and $\Delta y = 0.185$ m. Including the lateral boundaries, which are discretized with 7 nodes in the vertical direction, there are a total of 2,590 nodes and 2,320 cubic boundary elements. For a Courant number of 0.65, the initial time step is set to $\Delta t = 0.025$ s. Computations are run on a 1 GHz MAC-G4 and take 15'45" per time step. We run 199 (varying) time steps to reach $t = 4.2$ s. Numerical accuracy of the NWT solution is found to be good. Overall, the NWT volume is conserved to within 0.04%, and some of this is due to water exiting the NWT trough the open absorbing boundaries. The

discretized landslide volume is 0.00554 m^3 and varies by up to 1.2% during computations, as the landslide slides down the incline, due to discretization effects. The maximum error on mass conservation at any time step, based on integrated boundary fluxes, is 0.004% of landslide volume, which is quite small.

Nine numerical wave gages are specified in the NWT. Fig. 8 shows results computed at gages (a) and (b), as compared to experiments. We see that the agreement with the average experimental measurements is quite good for both gages. The differences in the shape of the first trough at gage (a) for $t \approx 0.5$ s are likely due to the effect of the small shelf at $x > 4.1$ m, which is not present in the experiments (Fig. 10).
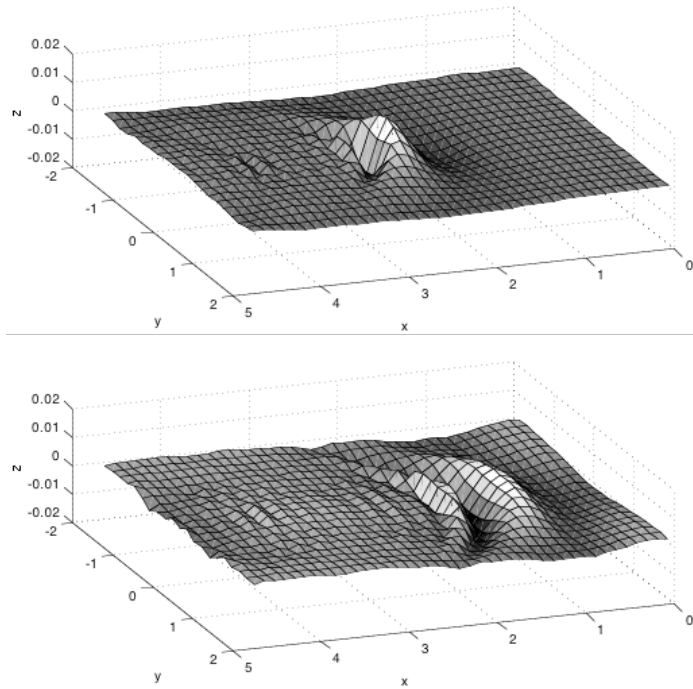

Fig. 11: Surface elevation of tsunami landslide computed at $t = 2.4$ s (above) and 4.2 s (below), with $d = 0.07$ m. Dimensions are in meter. Landslide motion and tsunami propagation are from left to right.

Fig. 11 shows 3D free surface elevation computed at $t = 2.4$ and 4.2 s. We see a leading trough and, behind it, a larger croissant shaped main crest, followed by a deeper trough and a smaller crest. Behind the latter, we see a tail of smaller oscillations. These are also visible in Fig. 8a. Overall, the leading waves are fairly directional and little lateral wave propagation occurs. These features are similar to those shown in Fig. 5.

Fig. 12 shows horizontal velocity u computed, from bottom to surface, under three gages located along the landslide axis ($y = 0$, $v = 0$), using eight internal points per gage. Results are shown up to $t = 2.8$ s, the instant where the landslide starts decelerating. Gage (a) coincides with gage (a) of Fig. 8a, i.e., it is located at the initial landslide location, and gage (b) is at the same distance from the origin as in Fig. 8b, but is located on the axis. Curves a-c in Fig. 12a show the flow above the landslide, when it is starting to move. The landslide then passes by the location of gage (b), for curves f-h in Fig. 12b, and gage (c), for curves h and i in Fig. 12c. All of these curves correspond to cases where the near bottom velocity is much larger, in absolute value, than velocities computed elsewhere in the water column, leading to horizontal velocity distributions that are quite non-uniform over depth.
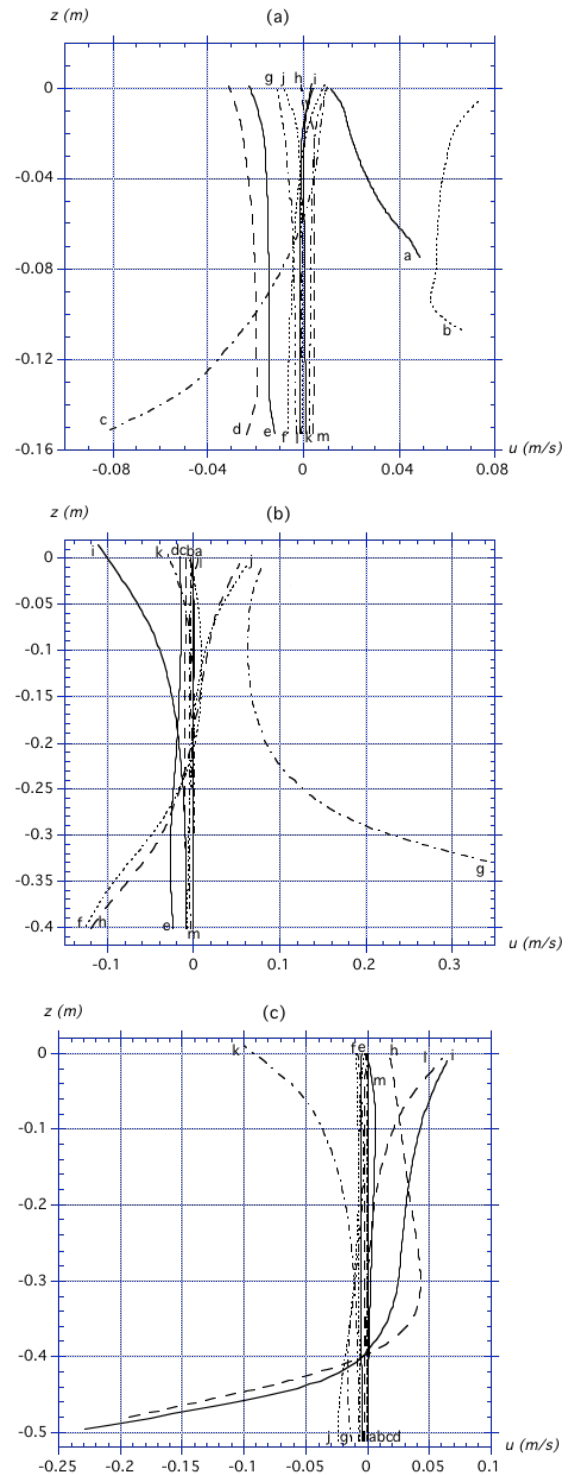

Fig. 12: Horizontal velocity computed along the landslide axis in the NWT, every 10 time steps, for $d = 0.070$ m, at gages located at : (a) $x = 3.754$ m, $y = 0$; (b) $x = 2.826$ m, $y = 0$ m; (c) $x = 2.411$ m, $y = 0$. Time of curves is $t =$ (a) 0.22; (b),0.47; (c) 0.69; (d) 0.89; (e) 1.10; (f) 1.31; (g) 1.52; (h) 1.73; (i) 1.94; (j) 2.15; (k) 2.37; (l) 2.56; (m) 2.77 s.

For the other curves in each figure, except for a few cases near the free surface, the horizontal velocity is quite uniform over depth, as would be expected from long wave theory.

CONCLUSIONS

The current experimental set-up is deemed satisfactory as far as the repeatability of landslide tsunami generation, for different runs with identical initial conditions. A preliminary comparison of one experimental configuration with computations in a 3D-NWT shows fairly good agreement for predicted surface elevations. Based on this, the NWT can be used to simulate landslide tsunami generation and analyze details of wave kinematics, such as internal velocities. A limited analysis of such horizontal velocities shows more complex velocity distributions above the moving landslide, than would be predicted by shallow water wave theories. Elsewhere, however, velocity is fairly uniform over depth, as would be expected for long propagating waves. These observations, together with the computer intensive nature of 3D-NWT computations, justify using a more efficient modeling methodology for landslide tsunami propagation. Thus, the authors have experimented with a coupled model, in which a tsunami source is first computed in the 3D-NWT, and then introduced in a long wave model for tsunami propagation over long distances (e.g., Watts et al, 2003).

We are currently in the process of testing other initial depths d for the landslide model and thus exploring different conditions of wave non-linearity and dispersion. Corresponding computations will be performed. In these additional tests, the symmetry of the measured wave field will allow us to position wave gages only on one side of the axis of symmetry and, as a consequence, to increase the number of measured data points per run. The optimal location of the wave gages will be determined with the help of the NWT, in order to provide the most meaningful data for model validation.

ACKNOWLEDGEMENTS

REFERENCES

Assier-Rzadkiewicz S., Mariotti C., and Heinrich P. (1997). "Numerical simulation of submarine landslides and their hydraulic effects," *J Wtrwy Port Coast Oc Engng*, Vol 123, No 4, pp 149-157.

Fine I.V., Rabinovich A.B., Kulikov E.A., Thompson R.E., and Bornhold B.D. (1998). "Numerical modeling of landslide-generated tsunamis with application to the Skagway Harbor tsunami of November 3, 1994," *Proc Tsunami Symp*, Paris.

Fryer G.J., Watts P., Pratson L.F. and Gardner J.V. (2001). "The tsunami of 1 April 1946: a landslide in the upper forearc," *Prediction of underwater landslide hazards,* Rotterdam: Balkema press.

Grilli S.T., and Watts P. (1999). "Modeling of waves generated by a moving submerged body: applications to underwater landslides," *Engng Analysis with boundary Elements*, Vol 23, No 8, pp 645-656.

Grilli S.T., Guyenne P., and Dias F. (2001). "A fully non linear model for three dimensional overturning waves over arbitrary bottom," *Int J of Numer Methods Fluids*, Vol 35, No 7, pp 829-867.

Grilli S.T., Vogelmann S., and Watts P. (2002). "Development of a 3D numerical wave tank for modeling tsunami generation by underwater landslides," *Engng Analysis with boundary Elements*, Vol 26, pp 301-313

Harbitz C.B. (1992). "Model simulations of tsunamis generated by the Storrega slides." *Marine Geol.*, Vol 105, pp 1-21.

Heinrich P. (1992). "Nonlinear water waves generated by submarine and aerial landslide," *J Wtrwy Port Coast Oc Engng.*, Vol 118, No 3, pp 249-266.

Iwasaki S. (1982). "Experimental study of tsunami generated by a horizontal motion of a sloping bottom," *Bull Earth Res. Inst.*, Vol 57, pp 239-262.

Iwasaki S. (1987). "On the estimation of a tsunami generated by underwater landslide," *Proc., Int. Tsunami Symp.,* Vancouver, B. C., pp 134-138.

Jiang L. and Leblond P.H. (1992). "The coupling of submarine slide and the surface waves which it generates," *J Geophys Res*, Vol 97(C8), pp 12731-12744.

Jiang L. and Leblond P.H. (1993). "Numerical modeling of an underwater Bingham plastic which it generates" *J Geophys Res*, Vol 98(C6), pp 10303-10317.

Jiang L. and Leblond P.H. (1994). "Three dimensional modeling of tsunami generation due to submarine mudslide," *J Phys Ocean*, Vol 24, pp 559-573.

Imamura F. and Gica E.C. (1996). "Numerical model for tsunami generation due to subaqueous landslide along a coast," *Sci Tsunami hazards,* vol 14, pp 13-28.

Murty T.S. (1979). "Submarine slide-generated water waves in Kitimat Inlet, British Columbia," *J Geophys Res*, Vol 84(C12), pp 7777-9.

Tappin D.R., Watts P., Mc Murtry G.M., Lafoy Y., Matsumoto T. (2001). "The Sissano, Papua New Guinea tsunami of July 1998 - offshore evidence on the source mechanism," *Marine Geol*, Vol 175, pp 1-23.

Verriere M. and Lenoir M. (1992). "Computation of waves generated by submarine landslides," *Int. J. Num. Methods Fluids*, Vol 14, pp 403-421.

Watts P. (1997). "Water waves generated by underwater landslides." *PhD thesis*, California Institute of Technology, Pasadena, CA.

Watts P. (1998). "Wavemaker curves for tsunamis generated by underwater landslides," *J Wtrwy Port Coast Oc Engng*, Vol 124 No 3, pp 127-137.

Watts P. (2000). "Tsunami features of solid block underwater landslides," *J Wtrwy Port Coast Oc Engng*, Vol 126, No 3, pp 144-152

Watts P. and Grilli S.T. (2003) "Tsunami generation by submarine mass failure Part I : Wavemaker models," *J Wtrwy Port Coast Oc Engng*. (submitted).

Watts P., Grilli S.T., and Kirby J.T. (2003) "Tsunami hazards at Skagway, Alaska," *J. Geophs. Res.* (submitted).

Wiegel R.L. (1955). "Laboratory studies of gravity waves generated by the movement of a submarine body," *Trans. Am. Geophys. Union*, Vol 36, No 5, pp 759-774.